Marko Mihalec
Department of Mechanical and Aerospace Engineering,
Rutgers University,
Piscataway, NJ 08854
e-mail: marko.mihalec@rutgers.edu

Mitja Trkov
Mem. ASME
Department of Mechanical Engineering,
Rowan University,
Glassboro, NJ 08028
e-mail: trkov@rowan.edu

Jingang Yi[1]
Fellow ASME
Department of Mechanical and Aerospace Engineering,
Rutgers University,
Piscataway, NJ 08854
e-mail: jgyi@rutgers.edu

Balance Recoverability and Control of Bipedal Walkers With Foot Slip

Low-friction foot/ground contacts present a particular challenge for stable bipedal walkers. The slippage of the stance foot introduces complexity in robot dynamics and the general locomotion stability results cannot be applied directly. We relax the commonly used assumption of nonslip contact between the walker foot and the ground and examine bipedal dynamics under foot slip. Using a two-mass linear inverted pendulum model, we introduce the concept of balance recoverability and use it to quantify the balanced or fall-prone walking gaits. Balance recoverability also serves as the basis for the design of the balance recovery controller. We design the within- or multi-step recovery controller to assist the walker to avoid fall. The controller performance is validated through simulation results and robustness is demonstrated in the presence of measurement noises as well as variations of foot/ground friction conditions. In addition, the proposed methods and models are used to analyze the data from human walking experiments. The multiple subject experiments validate and illustrate the balance recoverability concept and analyses. [DOI: 10.1115/1.4053098]

1 Introduction

Walking under foot-slip conditions often results in falling and slip-and-fall presents a major health risk, especially for elderly population [1]. The resulting injuries from fall-related incidences are the largest cause of economic burden among elderly, and the second largest in the general population [2]. Extensive research work have studied slip-and-fall problem from clinical perspectives with focus on experimental testing and analysis. For example, the work in Ref. [3] explored the benefits of training elderly individuals to walk on a slippery surface or treadmill. In Ref. [4], the stability of slip-induced gait in older adults was assessed as a function of the center of mass (CoM) and the contact between the foot and the ground was considered as a major factor. The different response in muscle actuation for expected and unexpected slip was demonstrated in Ref. [5]. A fast and reliable algorithm for slip detection in human walking was introduced, and the detection algorithm was built on bipedal dynamics [6].

Dynamic models are widely used in robotics research to study bipedal walking stability. Hybrid zero dynamics (HZD) is often used to describe and generate robotic bipedal gait [7]. Most of these modeling developments assume nonslip foot/ground contact. The HZD of human walking with foot slip was presented in Ref. [8], while Ref. [9] used HZD to create a stable gait of a bipedal robot with foot slippage. A compass gait with foot slip was analyzed in Ref. [10]. However, no analysis or balance control was designed in the above-mentioned research work. The synthesis of a stable nonslip gait was conducted using concepts such as the capture point [11]. The capture point defines a location on the ground where the zero moment point should be placed in order to stop the motion [12]. Capture point and zero moment point were used for slip controller in Ref. [13]. While they are useful for gait generation, those concepts however cannot be directly used to quantify the stability of the walker under arbitrary control. The capture point concept was also extended into the capturability regions [14], which give all the possible locations for foot placement to stop in a finite number of steps. Capturability regions were analyzed for an inverted pendulum model under foot slip [15]. While capturability considers the ability to stop, viability is described to avoid falling [16]. We extend the viability development in this work and design controllers to assist walkers to avoid fall under foot slip.

Using an inverted pendulum model has shown success in predicting many underlying characteristics of bipedal walkers [17–20]. Inverted pendulum-based models were also used to describe gaits with foot slip [13]. One of the most widely used inverted pendulum models is the linear inverted pendulum (LIP) model [21]. To retain the favorable properties, a two-mass LIP model was introduced and used for bipeds under foot slip [22,23]. The main advantage of the LIP model lies in its simplicity and thus analyses can be used to reveal the underlying fundamental principles. In Ref. [24], motion manifolds were introduced as geometric curves to define trajectories in the phase space for efficient optimization-based gait control. The work presented in this paper is inspired by the motion manifold concept for slip dynamics.

We use the two-mass LIP model to analytically obtain motion manifolds in the phase plane in the presence of foot slip. The dynamics are analyzed across different regions of the phase space such as safe, recoverable, and fall-prone regions. Built on these balance recoverability regions, an optimal control, a bang-bang controller, and a multi-step strategy are proposed. Simulation results are presented to validate and demonstrate analysis and control design. Both the dynamic model and the balance recoverability regions are applied to and compared with human experiments. The contributions of this work are threefold. First, we introduce and comprehensively analyze recoverability for walking gait under both nonslip and slip conditions. The new recoverability and motion manifold concepts provide an analytical tool to understand slip dynamics and gait stability. Second, a new recoverability region-based controller is proposed to successfully prevent bipedal walkers from fall. The use of motion manifold is new and provides an enabling tool to design balance recovery control under perturbations such as foot slip. Finally, we use the recoverability concept to analyze human-subject data. To the best of the authors' knowledge, this is the first time recoverability is applied to humanoids and verified by human subject data. Compared with previously presented conference publications [22,23], this work extends the recoverability with additional analyses, controller design, and extensive experimental and simulation results.

The remainder of the paper is organized as follows: Section 2 introduces the dynamic model and motion manifold. Section 3 presents and analyzes the recoverability regions. Section 4 uses

[1]Corresponding author.

Manuscript received July 19, 2021; final manuscript received November 11, 2021; published online January 21, 2022. Assoc. Editor: Sara Wilson.

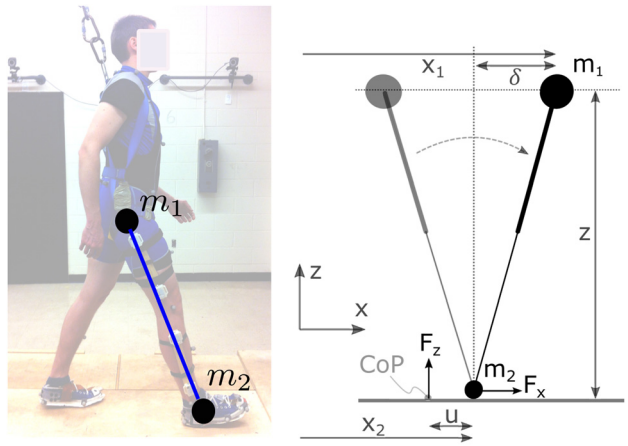

(*a*) (*b*)

Fig. 1 Two-mass inverted pendulum model in the sagittal plane: (*a*) human walking gait with two mass LIP and (*b*) schematic of the kinematics modeling setup

the recoverability concept to design the recovery controllers. The performance of the controller is demonstrated by simulations in Sec. 5. Section 6 uses human experiments to analyze stability and recoverability. Finally, concluding remarks are summarized in Sec. 7.

2 System Dynamics and Motion Manifolds

In this section, we first present the two-mass LIP model and then introduce the motion manifolds that will be used for recoverability analysis in the next section.

2.1 Dynamics Model. Figure 1(*a*) shows the simple setup of the two-mass LIP model for a human walker and Fig. 1(*b*) illustrates the modeling schematic. We consider only the walker's motion in the sagittal plane. The model includes two concentrated masses, m_1 and m_2, connected by a massless telescopic rod. The point mass m_2 is located at the point of contact between the foot and the ground and represents the mass of the standing leg below the knee. m_1 represents the mass of the rest of the body and is assumed to always maintain a constant height z above the ground. The horizontal positions of m_1 and m_2 are denoted by x_1 and x_2, respectively, with x_2 representing the location at the center of the stance foot. When the foot/ground contact is stationary, $\dot{x}_2 = \ddot{x}_2 = 0$, and m_2 is stationary.

The horizontal and vertical ground reaction forces are denoted as F_x and F_z, respectively. The horizontal distance between m_2 and the foot center of pressure (CoP) is defined as u and is considered as the walker's control input. u is positive when CoP is behind (posterior to) m_2 and negative when CoP is in front of m_2. The upper bound for the control input u is denoted as $u^{\max}$, namely, $-u^{\max} \le u \le u^{\max}$. The value of $u^{\max}$ depends on the joint torques such as ankle strength. The equation of motion for the two-mass LIP model is given as [22]

$$\ddot{x}_1 - \ddot{x}_2 = \frac{m_1 + m_2}{m_2 z}(x_1 - x_2 + u) + \frac{r_m g}{z}u - \frac{F_x}{m_2} \tag{1}$$

where constant $r_m = \frac{m_1+m_2}{m_1} > 1$ and g is the gravitational constant. We define the horizontal distance between the two masses as $\delta = x_1 - x_2$ and $\delta \ge 0$ when m_1 is in front of m_2 in the direction of walking. By taking $\ddot{x}_2 = 0$ in the absence of foot slip, the equation of motion is rewritten from Eq. (1) as

$$\ddot{\delta} = \omega^2(\delta + r_m u) \tag{2}$$

where constant $\omega = \sqrt{g/z}$. For the case when foot slip is present, $\dot{x}_2 > 0$, Coulomb friction model $F_x = -\mu F_z$ is used, where $F_z = (m_1 + m_2)g$ and μ is the foot/ground friction coefficient. Using Eq. (1), we obtain

$$\ddot{\delta} = \frac{m_1 + m_2}{m_2}\omega^2(\delta + r_m u + \mu z) \tag{3}$$

We write Eqs. (2) and (3) in a unified form as

$$\ddot{\delta} = \omega_m^2(\delta + A + r_m u) \tag{4}$$

with constants $A = 0$ and $\omega_m^2 = \omega^2$ for nonslip case and $A = \mu z$ and $\omega_m^2 = \frac{r_m}{r_m - 1}\omega^2$ under foot slip.

2.2 Motion Manifold. The advantage of using linear dynamics with the local coordinate variable δ is that Eq. (4) can be solved analytically and therefore enables the introduction of motion manifold. Given a set of initial conditions $(\delta_0, \dot{\delta}_0)$ and under constant input $u = u_0$, the solution to Eq. (4) is obtained

$$\delta(t) = \frac{\dot{\delta}_0}{\omega_m}\sinh(\omega_m t) + (\delta_0 + A + r_m u_0)\cosh(\omega_m t) - A - r_m u_0 \tag{5}$$

and its derivative

$$\dot{\delta}(t) = \dot{\delta}_0\cosh(\omega_m t) + \omega_m(\delta_0 + A + r_m u_0)\sinh(\omega_m t) \tag{6}$$

We rewrite the above solution in form of a relationship between δ and $\dot{\delta}$ without explicit time t. The motion manifold $\mathcal{M}$ is presented as a curve in the δ-$\dot{\delta}$ plane. By using Eqs. (5) and (6) and noting the identity $\cosh^2(x) - \sinh^2(x) = 1$, the motion manifold $\mathcal{M}$ for Eq. (4) is obtained as

$$\mathcal{M}: \ \omega_m^2(\delta^2 - \delta_0^2) + 2(A + r_m u_0)\omega_m^2(\delta - \delta_0) + \dot{\delta}_0^2 - \dot{\delta}^2 = 0 \tag{7}$$

and we arrange the above equation as

$$\mathcal{M}: \ \frac{(\delta + A + r_m u_0)^2}{(\delta_0 + A + r_m u_0)^2 - \frac{\dot{\delta}_0^2}{\omega_m^2}} - \frac{\frac{\dot{\delta}^2}{\omega_m^2}}{(\delta_0 + A + r_m u_0)^2 - \frac{\dot{\delta}_0^2}{\omega_m^2}} = 1 \tag{8}$$

Manifold $\mathcal{M}$ captures the implicit time dependence between δ and $\dot{\delta}$ and their motion direction (vector field). Equation (8) represents a family of hyperbolic curves with foci on the abscissa where each set of initial conditions $(\delta_0, \dot{\delta}_0)$ defines a single hyperbola. Figure 2 shows a family of motion manifolds $\mathcal{M}$ to illustrate the general shapes. In the cases of constant u and the absence of any external perturbation, the dynamics of the system follows $\mathcal{M}$ in the phase plane. Motion manifolds obtained under zero actuation $u_0 = 0$ are called nominal manifolds.

To analyze the relationship between an arbitrary state and a given manifold, we introduce a measure of Riemann distance from the nominal manifold $\mathcal{M}$, denoted by σ. The value σ is inspired from Ref. [24] and is taken from the left side of Eq. (7) with $u_0 = 0$ as

$$\sigma = \omega_m^2\delta^2 + 2\delta A\omega_m^2 - \dot{\delta}^2 + \dot{\delta}_0^2 - \delta_0^2\omega_m^2 - 2A\delta_0\omega_m^2 \tag{9}$$

Note that $\sigma = 0$ denotes zero deviation and in this case (9) yields the nominal manifold. By using motion manifold $\mathcal{M}$ and metric σ, the problem of solving a differential equation given in Eq. (4) is transformed into a significantly simplified geometric problem of choosing the appropriate manifolds $\mathcal{M}$ governed by the algebraic equation in Eq. (8). The recovery control problem is then related to regulating σ to zero.

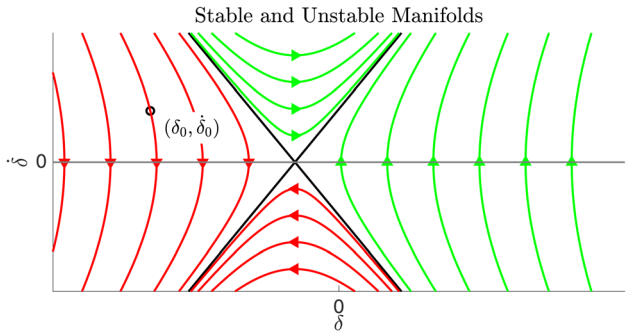

Fig. 2 Nominal manifolds for various initial conditions $(\delta_0, \dot{\delta}_0)$ with same parameter $A > 0$. The intersection of the two straight asymptotes defines the saddle point $(-A, 0)$. The manifolds converging towards the first quadrant (green) represent forward progression of CoM, while the ones converging to the third quadrant (red) lead toward backward fall.

3 Balance Recoverability Under Foot Slip

This section introduces and defines the concept of balance recoverability. As shown in Fig. 2, while some initial states allow the walker to maintain forward progression (i.e., curves converging towards the first quadrant), others inevitably lead to falling (i.e., curves converging to the third quadrant). Each set of initial conditions $(\delta_0, \dot{\delta}_0)$ uniquely defines a manifold and the walker deviates from the manifold in the case of external perturbations or under control input u. We can quantify and distinguish these manifolds. For example, these green-colored manifolds in the figure are considered stable since a walker with states on them maintains forward progression, while red-colored manifolds are unstable, as the walker does not maintain forward progression and eventually starts falling backward relative to the stance foot. The recoverability regions define such differences.

3.1 Balance Recoverability Regions. The sets of motion manifolds yielding qualitatively different gait stability are encompassed in the definition of balance recoverability regions as follows.

DEFINITION 1 (Balance recoverability regions). *A bipedal walker with nominal manifold (9) and initial condition $(\delta_0, \dot{\delta}_0)$ at t_0 is within the* **safe region** *$\mathcal{R}^s$ if its nominal manifold $\mathcal{M}$ is a hyperbola with positive $\dot{\delta}$ or a conjugate hyperbola with positive $\dot{\delta}$; within a* **recoverable region** *$\mathcal{R}^r$ if there exists a feasible control input u and time $t_1 > t_0$ under which its states enter $\mathcal{R}^s$ at t_1; and within a* **fall-prone region** *$\mathcal{R}^f$ if its states lie outside $\mathcal{R}^r \cup \mathcal{R}^s$.*

Within a single foot step, it is possible to transit between different regions. Depending on the control input, a walker in recoverable region $\mathcal{R}^r$ can stay within $\mathcal{R}^r$, or it can transit to either $\mathcal{R}^s$ or $\mathcal{R}^f$. Under foot slip, a walker in $\mathcal{R}^s$ can keep within $\mathcal{R}^s$ or transit to $\mathcal{R}^f$. A walker in $\mathcal{R}^f$ would have to stay within $\mathcal{R}^f$ unless additional recovery steps are taken or the foot/ground contact becomes nonslipping.

To precisely compute the recoverability regions in the above definitions, the separation lines $\mathcal{B}^{\mathrm{sr}}$ and $\mathcal{B}^{\mathrm{rf}}$ are defined as the interfacing boundaries between the recoverable region $\mathcal{R}^r$ and the safe and the fall-prone regions ($\mathcal{R}^s$ and $\mathcal{R}^f$), respectively. The separation line between $\mathcal{R}^s$ and $\mathcal{R}^r$ is obtained as an asymptote of the nominal dynamics hyperbola (i.e., $u = 0$)

$$\mathcal{B}^{\mathrm{sr}} = \{(\delta, \dot{\delta}) : \dot{\delta} = -\omega_m(\delta + A)\} \tag{10}$$

Control input $u = u^{\max}$ is used for computing the separation line $\mathcal{B}^{\mathrm{rf}}$ between $\mathcal{R}^r$ and $\mathcal{R}^f$. Plugging $u^{\max}$ into Eq. (8) yields the expression for $\mathcal{B}^{\mathrm{rf}}$

$$\mathcal{B}^{\mathrm{rf}} = \{(\delta, \dot{\delta}) : \dot{\delta} = -\omega_m(\delta + A + r_m u^{\max})\} \tag{11}$$

Using the above calculations, the safe, recoverable, and fall-prone regions are then captured as follows:

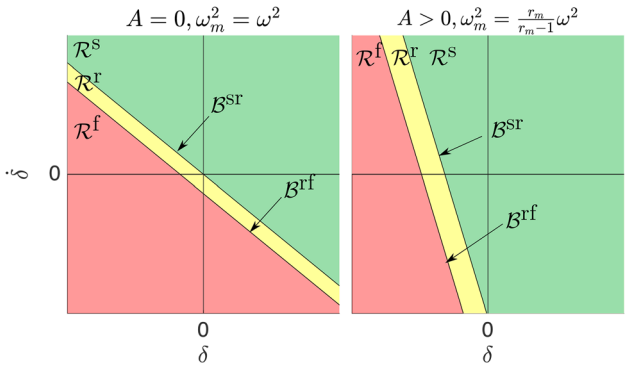

Fig. 3 Safe ($\mathcal{R}^s$), recoverable ($\mathcal{R}^r$), and fall-prone ($\mathcal{R}^f$) regions. Left: normal walking without slip, right: in presence of foot-slip.

$$\mathcal{R}^s = \{(\delta, \dot{\delta}) : \dot{\delta} \geq -\omega_m(\delta + A)\} \tag{12a}$$

$$\mathcal{R}^r = \{(\delta, \dot{\delta}) : -\omega_m(\delta + A + r_m u^{\max}) \leq \dot{\delta} < -\omega_m(\delta + A)\} \tag{12b}$$

$$\mathcal{R}^f = \{(\delta, \dot{\delta}) : \dot{\delta} \leq -\omega_m(\delta + A + r_m u^{\max})\} \tag{12c}$$

Figure 3 shows the schematics of the regions and corresponding separation lines. We now present a result that justifies the above use of $u^{\max}$ in Eqs. (11), (12*b*), and (12*c*) to compute the boundaries of regions $\mathcal{R}^s$, $\mathcal{R}^r$, and $\mathcal{R}^f$.

LEMMA 1. *The recoverability regions $\mathcal{R}^r$ and $\mathcal{R}^f$ are obtained under the maximum control input $u = u^{\max}$.*

Proof. We prove the results by contradiction. Suppose that the recoverable region $\mathcal{R}^r$ is given by a control input $u_1 < u^{\max}$. The boundary $\mathcal{B}^{\mathrm{rf}}$ is given by $\dot{\delta} = -\omega_m(\delta + A + r_m u_1)$. Let us then consider a point B with coordinate $(\delta_2, \dot{\delta}_2)$ in the phase plane such that $-\omega_m(\delta_2 + A + r_m u^{\max}) < \dot{\delta}_2 < -\omega_m(\delta_2 + A + r_m u_1)$. It is straightforward to obtain that B lies outside the recoverable region $\mathcal{R}^r$ defined by u_1. However, if applying the control input $u^{\max}$, the dynamics follow a conjugate hyperbola and according to Definition 1, point B belongs to $\mathcal{R}^r$, thus resulting in contradiction. Similar reasoning can be used for $\mathcal{R}^f$. ■

3.2 Recoverability Regions Under Nonslip/Slip Conditions. In order to understand the change in dynamics at the onset or termination of foot slip, we analyze the possible transitions between two recoverability regions. The dynamic models under nonslip and slip cases are different and therefore, the defined recoverability regions are not the same under these two conditions. We thus need to know the relationships among the recoverability regions under nonslip and slip gaits.

Under a sudden foot slip, a set of possible transitions happen between normal nonslip walking recoverability regions $\mathcal{R}_n^s$, $\mathcal{R}_n^r$, or $\mathcal{R}_n^f$ and those regions $\mathcal{R}_{sl}^s$, $\mathcal{R}_{sl}^s$, or $\mathcal{R}_{sl}^f$ under slip condition. Subscripts "n" and "sl" are used to denote the nonslip and slip walking cases, respectively. Since the onset of slip is instantaneous, state variables $(\delta, \dot{\delta})$ remain the same right before and after foot slip. Because the regions change instantaneously under nonslip or slip cases, the same point in the phase plane might transit to a different region under the new condition. To quantify the possible transitions, Fig. 4 illustrates the overlaid two sets of recoverability regions under nonslip and slip conditions. We focus on the second quadrant of the δ-$\dot{\delta}$ plane as this is the beginning of the stance step where slip occurs.

By examining Eqs. (10) and (11), it is clear that two pairs of boundary lines $\mathcal{B}_{\mathrm{i}}^{\mathrm{sr}}$ and $\mathcal{B}_{\mathrm{i}}^{\mathrm{rf}}$ are parallel, $i = \mathrm{sl}, \mathrm{n}$. Furthermore, note that $\omega_m^2 \geq \omega^2$, these two sets of parallel boundary lines intersect at four points, denoted as $P_1 = \mathcal{B}_n^{\mathrm{rs}} \cap \mathcal{B}_{sl}^{\mathrm{rf}}$, $P_2 = \mathcal{B}_n^{\mathrm{rs}} \cap \mathcal{B}_{sl}^{\mathrm{rs}}$,

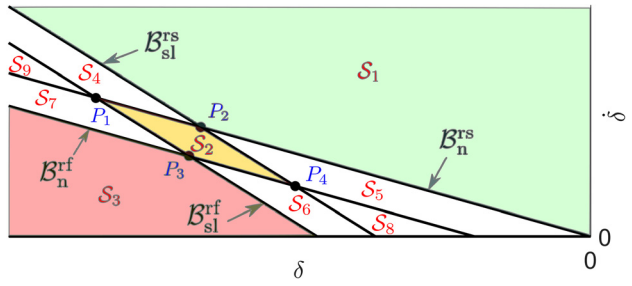

Fig. 4 Overlapping the boundary lines and the three recoverability regions for presence and absence of foot slip reveals the set of four intersection points P_i, $i = 1, 2, 3, 4$, and nine distinct sets $\mathcal{S}_j$, $j = 1, \ldots, 9$

$P_3 = \mathcal{B}^{rf}_n \cap \mathcal{B}^{rf}_{sl}$, and $P_4 = \mathcal{B}^{rf}_n \cap \mathcal{B}^{rs}_{sl}$; see Fig. 4. Points P_1, P_2, and P_3 always appear in the second quadrant, while the location of P_4 depends on model parameters values. By using Eqs. (10) and (11) for the boundary lines and substituting the corresponding values for the slip and nonslip cases, the coordinates for the four intersection points are obtained as follows:

$$P_1(-r_\omega(\mu z + r_m u^{\max}),\ r_\omega\omega(\mu z + r_m u^{\max}))$$
$$P_2(-r_\omega\mu z,\ r_\omega\omega\mu z),\ P_3(-r_\omega\mu z - r_m u^{\max},\ r_\omega\omega\mu z)$$
$$P_4\left(-r_\omega\left(\mu z - r_m u^{\max}\sqrt{1-\frac{1}{r_m}}\right),\ r_\omega\omega(\mu z - r_m u^{\max})\right)$$

where $r_\omega = r_m(1 + \sqrt{1 - \frac{1}{r_m}}) > 1$.

The two pairs of parallel boundary lines partition the second quadrant of the δ-$\dot{\delta}$ plane into nine distinct sets, denoted as $\mathcal{S}_1, \ldots, \mathcal{S}_9$ as shown in Fig. 4. Note that P_4 represents the upper limit of intersection region $\mathcal{S}_8 = \mathcal{R}^f_n \cap \mathcal{R}^s_{sl}$. Therefore, when P_4 is located below the abscissa line $\dot{\delta} = 0$, the two regions do not intersect, that is, $\mathcal{S}_8 = \varnothing$. In other words, if $\mu z \le r_1 u^{\max}$, keeping the model within $\mathcal{R}^s_{sl}$ becomes a sufficient condition to avoid both fall-prone regions $\mathcal{R}^f_{sl}$ and $\mathcal{R}^f_n$. This observation is helpful for designing a recovery strategy. Since the condition $\mu z \le r_1 u^{\max}$ relies solely on the ground friction condition and the maximum control capabilities $u^{\max}$, neither of these parameters is controllable by the walker and therefore, cannot be used in the balance control strategy.

To design a safe gait, a particular interest should be given to set $\mathcal{S}_1$ that represents the intersection of the safe sets for slip and nonslip cases, i.e., $\mathcal{S}_1 = \mathcal{R}^s_n \cap \mathcal{R}^s_{sl}$. For a walker within $\mathcal{S}_1$, it is safe regardless of slip status. Therefore, $\mathcal{S}_1$ is always preferred and serves as a target set for the controller. We express $\mathcal{S}_1$ as follows:

$$\mathcal{S}_1 = \left\{(\delta, \dot{\delta}) : \dot{\delta} \ge \max\left(-\omega\sqrt{\frac{r_m}{r_m - 1}}(\delta + \mu z), -\omega\delta\right)\right\} \quad (13)$$

Conversely, set $\mathcal{S}_3 \cup \mathcal{S}_6 \cup \mathcal{S}_7 \cup \mathcal{S}_8 \cup \mathcal{S}_9 = \mathcal{R}^f_n \cup \mathcal{R}^f_{sl}$ encompasses fall-prone regions and therefore the walker should always avoid this set.

4 Balance Recovery Control

Considering the aforementioned recoverability region analysis, we present a recovery controller design. To maintain walker's stability, two types of strategies are taken: a continuous within-step (i.e., one step) control u or multi-step recovery control. A combination of these two strategies is also used to help optimize the foot placement in additional recovery steps. The decision about the control strategy is based on the recoverability estimation such that a recovery step is taken only when the within-step control is insufficient to maintain balance. Figure 5 illustrates the flowchart of the recovery control strategies. In the following, we first present

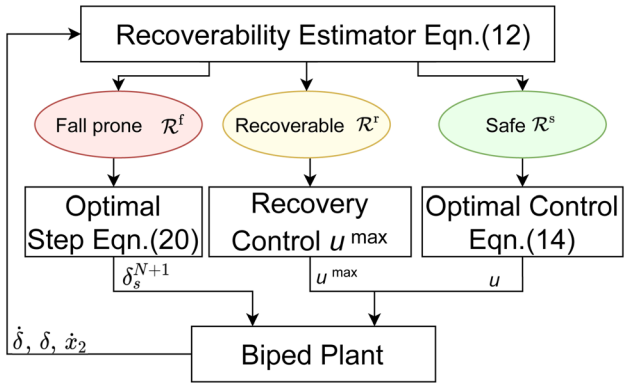

Fig. 5 Flowchat of the controller design. The current walker's state is evaluated in terms of recoverability and in turn determines the appropriate control strategies.

the within-step control design and then multi-step recovery strategies.

4.1 Within-Step Recovery Control. When current state $(\delta, \dot{\delta})$ lies in $\mathcal{R}^s$, it is not prone to backward fall. For this case, we design an optimization-based control u that minimizes the deviation from the desired nominal manifold as well as the control effort. Given the target state $(\delta_t, \dot{\delta}_t)$, the control u^* is given by solving the following optimization problem:

$$u^* = \underset{u}{\operatorname{argmin}}\, C_w = \underset{u}{\operatorname{argmin}}\left[W_t\sigma_t^2 + \int_\delta^{\delta_t}(W_d\sigma^2 + W_i u^2)d\delta\right] \quad (14)$$

where cost $C_w = W_t\sigma_t^2 + \int_\delta^{\delta_t}(W_d\sigma^2 + W_i u^2)d\delta$ is computed in the δ-$\dot{\delta}$ space. In Eq. (14), σ_t represents a terminal cost, which is a metric of the distance of $(\delta, \dot{\delta})$ to the target manifold at the point of nominal step transition. W_t, W_d, and W_i are the weights related to the terminal cost, deviation from the desired trajectory, and the control input, respectively. The deviation σ from the target manifold is obtained by substituting $(\delta_0, \dot{\delta}_0)$ in Eq. (9) with $(\delta_t, \dot{\delta}_t)$, namely,

$$\sigma = \delta^2\omega_m^2 - \delta_t^2\omega_m^2 + 2\delta A\omega_m^2 - 2A\delta_t\omega_m^2 + \dot{\delta}_t^2 - \dot{\delta}^2 \quad (15)$$

To efficiently obtain the solutions to Eq. (14) for real-time applications, we build a precalculated look-up table offline and use it online. Using the configuration variable δ in the local coordinate system and the deviation σ from the target motion manifold, the calculation of the look-up table does not need to be repeated for every time-step due to the generalized treatment of the dynamic model (9). Therefore, a single table in the δ-σ space provides the optimal control input u for any combination of the current $(\delta, \dot{\delta})$ and target states $(\delta_t, \dot{\delta}_t)$. This is one of the attractive features of using the motion manifold.

We now present how to obtain the target state $(\delta_t, \dot{\delta}_t)$. The target state uniquely defines a single hyperbolic manifold in Eq. (8). For a walker in the safe region, i.e., $(\delta, \dot{\delta}) \in \mathcal{R}^s$, the goal is to return to periodic walking, which is characterized by a desired CoM velocity. Since the velocity $\dot{\delta}$ changes throughout the gait, we define the mean CoM velocity $\bar{\dot{\delta}}$ as the average of $\dot{\delta}$ during a single step manifold in the δ-$\dot{\delta}$ space. We denote the beginning and the end points of a periodic walk step as δ_s and $-\delta_s$, respectively. Using Eq. (8) with $u_0 = 0$, $\dot{\delta}$ is then calculated over $[\delta_s, -\delta_s]$ as

$$\bar{\dot{\delta}} = \frac{1}{2\delta_s}\int_{\delta_s}^{-\delta_s}\sqrt{\omega_m^2\delta^2 + \dot{\delta}_{\text{apex}}^2 + 2A\omega_m^2\delta}\,d\delta \quad (16)$$

where $\dot{\delta}_{\text{apex}}$ is the apex velocity, that is, the velocity at $\delta = 0$. Given the desired walking velocity $\bar{\dot{\delta}}$, we use Eq. (16) to solve

$\dot{\delta}_{\text{apex}}$ numerically. This would give the target state as $(\delta_t, \dot{\delta}_t) = (0, \dot{\delta}_{\text{apex}})$, which is used in Eq. (14) to obtain the optimal control input u^*.

If the current state is in the recoverable region, i.e., $(\delta, \dot{\delta}) \in \mathcal{R}^r$, the gait would result in a backward fall. To prevent the fall and ensure maximum robustness, we propose a bang-bang type control where a maximum control input $u^{\max}$ is applied. According to Lemma 1, $u^{\max}$ is necessary and sufficient for returning to $\mathcal{R}^s$ from any point in $\mathcal{R}^r$. If the walker's current state is in the fall-prone region, i.e., $(\delta, \dot{\delta}) \in \mathcal{R}^f$, within-step recovery is impossible. Nevertheless, it would be beneficial for the overall recovery sequence by applying maximum control input $u^{\max}$ because it maintains the minimum deviation σ between the current manifold and the recoverability boundary $\mathcal{B}^{\text{rf}}$. This would generate maximum time duration before fall and thus allow the swing foot possibly enough time to position itself and prevent the fall with taking additional steps as we discuss in the next section.

4.2 Multi-Step Foot Placement and Control. While a fall-prone state cannot avoid falling using only the within-step control, balance recovery is possible by taking additional steps. In this case, target state $(\delta_t, \dot{\delta}_t)$ needs to be specified. For the nonslip gait, the origin is often specified as the target state and is commonly used in capturability-based analysis [14]. We generalize this approach by specifying the target as a stationary point in the phase portrait. For the two-mass LIP model, the only stationary point in the phase portrait is the saddle point; see Fig. 2. For a model under foot-slip, the saddle point is defined as $(-A, 0)$. Reaching the saddle point as the target allows a slipping model to maintain constant state $(\delta, \dot{\delta})$ for prolonged time while the slipping foot is decelerating.

To characterize the manifold, we consider the intersection of $\mathcal{M}$ and the coordinate axis. For a walker in $\mathcal{R}^f$, we define δ_{vertex} as the point where the current manifold crosses the abscissa and the forward progression of the model stops (i.e., $\dot{\delta} = 0$). Therefore, from Eq. (8) with $u_0 = 0$, we obtain δ_{vertex} as

$$\delta_{\text{vertex}} = -A - \sqrt{(\delta + A)^2 - \frac{\dot{\delta}^2}{\omega_m^2}} \tag{17}$$

The goal of the step location planer is to transit the walker from the current manifold with $(\delta_{\text{vertex}}, 0)$ to the target manifold with $(-A, 0)$. In general, we consider the case of N-step recovery sequence, $N \in \mathbb{N}$, and each step is designed to decrease the distance between $(\delta_{\text{vertex}}, 0)$ and $(-A, 0)$ proportionally by $1/N$. Therefore, the target configuration for each subsequent step in the N-step recovery sequence is denoted by the point $\boldsymbol{x}_t^N$ with coordinates as

$$\boldsymbol{x}_t^N = \left(-A + \frac{(N-1)}{N}(\delta_{\text{vertex}} + A),\ 0 \right) \tag{18}$$

Figure 6 illustrates the schematics and examples of one-step and two-step recovery. Each step represents a horizontal jump in the δ-$\dot{\delta}$ plane, denoted by a horizontal dashed line. In this example, $A = 0$ and the target configuration is $(\delta_t, \dot{\delta}_t) = (0, 0)$. The one-step recovery commands the trailing leg to make a longer step backward, bringing the model onto the nominal manifold through the target configuration. For the two-step recovery, the intermittent step is selected such that the vertex distance of the intermittent step is one half of the vertex distance before the step is taken.

When a step is taken from within the safe region $\mathcal{R}^s$, a recovery to periodic walk is considered. Manifolds within $\mathcal{R}^s$ only intersect with the ordinate, which we denote by $\dot{\delta}_{\text{apex}}$. Similarly as in the above description, in this case, each step in the N-step recovery sequence to periodic gait is specified by coordinates as

$$\boldsymbol{x}_t^N = \left(0,\ \dot{\delta}_{t,\text{apex}} + \frac{(N-1)\left(\dot{\delta}_{\text{apex}} - \dot{\delta}_{t,\text{apex}}\right)}{N} \right) \tag{19}$$

where $\dot{\delta}_{t,\text{apex}}$ is the target apex velocity by solving (16).

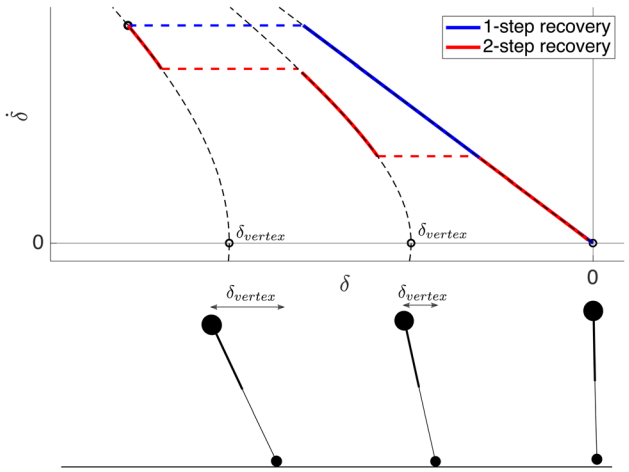

Fig. 6 Multi-step recovery from $\mathcal{R}^f$. Top: one-step and two-step and the corresponding vertex velocities. Bottom: schematics of the model when $\dot{\delta} = 0$ shows the vertex configuration.

Taking a step represents a discrete and instantaneous jump in δ. The location of the Nth step is given by δ_s^N, the configuration of the model immediately after taking the Nth step. δ_s^N is initially calculated as a horizontal distance between the current state δ and the target manifold specified by $\boldsymbol{x}_t^N$ defined in either (18) or (19). The actual stepping location $\boldsymbol{x}_t^N$ is subsequently refined by solving the following optimization problem which reduces to the need for within-step control:

$$\delta^* = \underset{\delta_s^N}{\text{argmin}} \left(C_w(\delta,\ \delta_t) + W_s(\delta_s^N - \delta_s^{N-1})^2 \right) \tag{20}$$

where C_w is the cost associated with the continuous control design given in (14), and W_s is the weight of the cost of changing the planned location. The difference of $\delta_s^N - \delta_s^{N-1}$ is included to penalize the variation of the states at the beginning of the consecutive steps. This term ensures that the model avoids excessive variations and prefers periodic gaits.

5 Simulation Results

We conduct simulation studies to validate and demonstrate the analyses and control design. We tailor the parameters of a two-mass LIP model to accurately represent human anatomy. From Ref. [25], the foot and the shank account for 1.45% and 4.65% of the whole body mass, respectively. Therefore, the ratio of the masses in the model is given as $m_1/m_2 = 15.39$. The vertical distance between the ground and point mass m_1 is defined as $z = 0.55H$, where H represents the person's height. A height of $H = 1.73$ m is used in simulation to match the average height of the subjects performing the experiments as described in the next section. The maximum control input is considered to be $u^{\max} = 5$ cm, which is taken from the experiments reported in Ref. [26].

Figure 7 shows two examples that demonstrate the within-step controller performance. In the first case, the initial velocity $\dot{\delta}_0$ (red-colored solid line) is higher than the desired value (dash line) while the second case depicts a velocity (blue-colored solid line) lower than the desired value. The nominal manifold running through the target state is denoted as the target manifold. We also plot σ as the distance from the target manifold and its values converge to zero rapidly. The plot also includes the control input u. The line $\sigma = 0$ in the δ-σ plane clearly describes the trajectory convergence under the control.

Figure 8 demonstrates the performance of the within-step control under model and measurement noises and variations. Figure 8(*a*) shows the performance of the within-step controller under model errors and random noise. A simulation of slipping

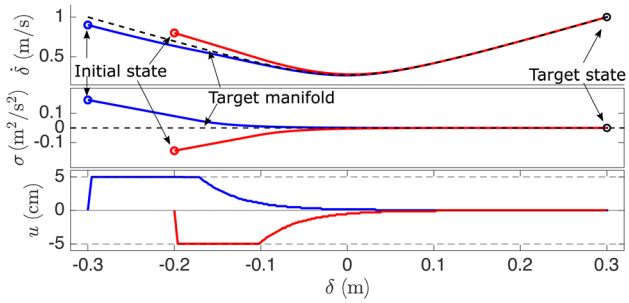

Fig. 7 Performance of controller converging the model to target manifold. Top: evolution in the δ-$\dot{\delta}$ phase space. Middle: the same evolution in $\delta-\sigma$ space. Bottom: control input u.

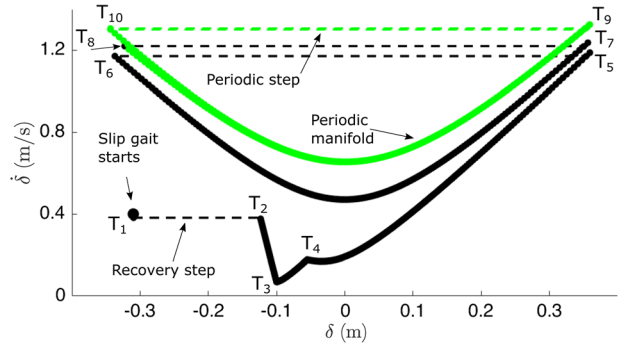

Fig. 9 Multi-step recovery sequence: T_1: unstable slipping within $\mathcal{R}^f_{sl}$ initiates recovery step to T_2. T_2–T_3: stable slipping in $\mathcal{R}^s_{sl}$, T_3–T_8: recovery to periodic gait without foot slip, T_9–T_{10}: periodic walking without foot slip in $\mathcal{R}^s_n$.

gait is set in motion at the point $\delta_0 = -0.25$ m with the velocity lower than the desired value. In the figure, the dashed curve represents a nominal manifold through a preselected target state. Given the knowledge of the current and target states, the optimal controller guides the model (red curve) to converge to the desired manifold (dashed line). The simulation is repeated with added noises to the estimates of both δ and $\dot{\delta}$ (i.e., measurement noises). Even with the noises, the controller demonstrates robustness by successfully converging toward the nominal target manifold rapidly.

Figure 8(*b*) shows the control performance with uncertain ground contact friction. The red curve shows the performance of the controller using the actual foot/ground friction coefficient $\mu = 0.1$. Two other simulation runs are conducted with $\pm 20\%$ variations of the actual μ value as the friction estimates in the control. In all cases, the system achieves to converge to the desired target states. However, inaccurate information about μ increases the control effort as the model does not follow the nominal manifold. In terms of balance recoverability, underestimating μ is considered as a safe option. This can be seen in Fig. 8(*b*), where for each δ, the velocity $\dot{\delta}$ with estimated $\mu = 0.08$ is higher than that in the case with estimate $\mu = 0.12$.

Figure 9 shows the performance of the multi-step slip recovery control. The model is set in motion with foot slip at the state $(\delta, \dot{\delta}) = (-0.3, 0.4)$, which lies in the fall-prone region. The control algorithm selects the saddle point $(-A, 0) = (-0.1, 0)$ as the target state and initiates a recovery step. Since a behind/posterior recovery step is taken, δ increases and the step is depicted in the δ-$\dot{\delta}$ plane as a horizontal jump from T_1 to T_2 in the figure. After the step, the walker is in the safe region $\mathcal{R}^s_{sl}$ and the within-step controller is used to return to the target state $(-A, 0) \in \mathcal{R}^s_{sl}$. As the contact foot comes to rest, $\dot{x}_2 = 0$, the slip stops (at T_3). By the schematics in Fig. 4, $T_3 \in \mathcal{S}_5$ and the transition $\mathcal{R}^s_{sl} \rightarrow \mathcal{R}^r_n$ happens. Under the controller, the gait returns to the safe region $T_4 \in \mathcal{R}^s_n$ and periodic motion is then recovered. Gaits T_5 to T_8 characterize the recovery steps toward periodic gaits T_9 and T_{10}. All T_4-T_{10} are in safe region $\mathcal{R}^s_n$.

6 Human Experiments

6.1 Results. We further take human subject data to demonstrate the modeling and recoverability framework. Eight healthy young subjects (26 ± 3 years old) were recruited to take slip-and-fall experiments. Subjects were outfitted with a harness system to prevent them from hitting the ground in case of a fall but did not affect their movement under foot slip. Subjects were instructed to repeatedly walk on a wooden platform at a comfortable self-selected pace. After the subjects were comfortable with the setup, unbeknownst to them, the ground conditions were changed by applying lubricant to a patch of smooth polymer surface in the middle of the walkway to create foot-slip gait. A motion capture system was used to obtain the kinematic data of the subjects and these data were later processed to extract the CoM and foot/ground contact point kinematics. The approval for the study was granted by the Institutional Review Board at Rutgers University. The detailed experiment setup is described in Ref. [26].

Figure 10(*a*) presents the δ-$\dot{\delta}$ trajectory of the multi-subject experiments for both nonslip and slip cases. Due to different self-selected paces, the velocity is normalized with the average velocity $\dot{\delta}$ of normal nonslip gait and δ is normalized by the height of subject's CoM. Figure 10(*b*) shows the recoverability analysis of the human-subject gaits. The results match the model predictions as all the normal gaits are in safe region $\mathcal{R}^s_n$. Conversely, due to exceptionally low friction coefficient (around $\mu = 0.1$), all of the slip cases are in fall-prone region $\mathcal{R}^f_{sl}$. While some subjects were successful in avoiding fall, they did so by either taking additional recovery steps, or by allowing their slipping foot to slide off of the slippery portion of the platform with encountered increased friction. None of the subjects was able to avoid fall without taking a step or experiencing increased friction.

We take a detailed look at one of the successful recovery experimental trial. Figure 11(*a*) shows the snapshots of a single trial,

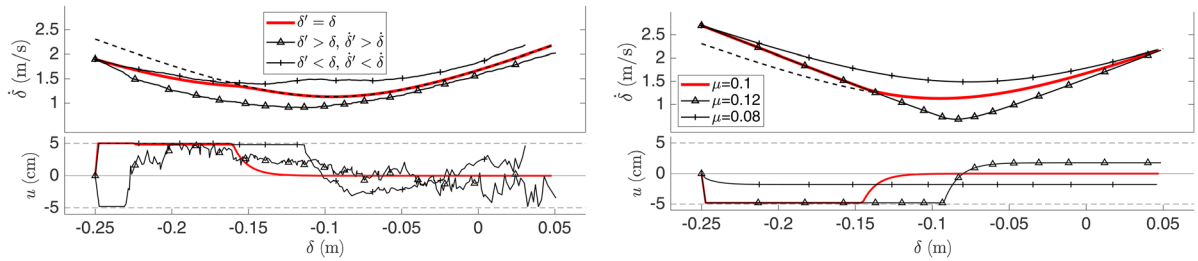

(*a*) (*b*)

Fig. 8 (*a*) Effects of estimation error and noise on controller performance. $\delta' = \delta \pm 0.02$ m, $\dot{\delta}' = \dot{\delta} \pm 0.4$ m/s. (*b*) Performance of the controller in the case of inaccurate friction coefficient μ. Top: evolution of the model through phase space with accurate, underestimated, and overestimated μ. Bottom: control effort is reduced if the friction coefficient used by the controller matches the true value.

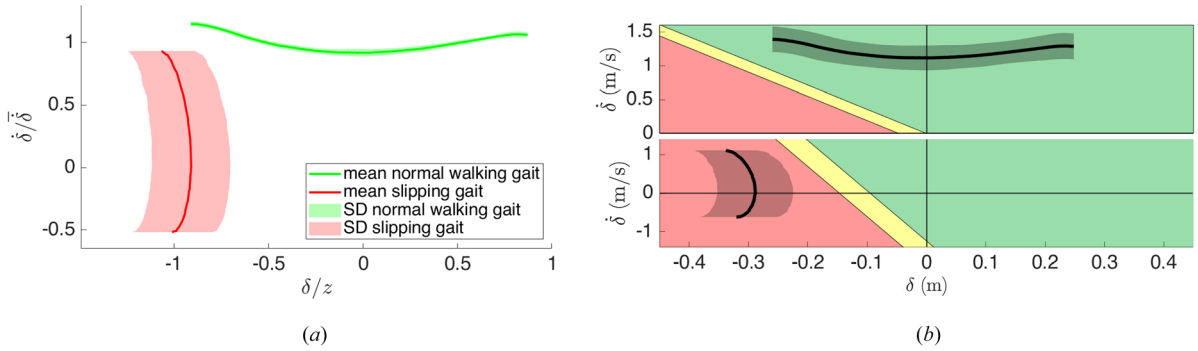

(*a*) (*b*)

Fig. 10 (*a*) Normal walking and slipping gaits for multiple subjects. Solid lines represent mean values while the shaded area represents the standard deviation across multiple subjects. The axes are normalized so that the gaits with different paces are comparable. (*b*) Experimental results compared to balance recoverability regions. Solid lines represents the mean, while the shaded area represents the standard deviation of multiple subjects' results. Top: normal walking gaits without foot slip are a part of the safe region $\mathcal{R}^s_n$. Bottom: at the onset of slip, the region boundaries change and all slipping gaits are within the fall-prone region $\mathcal{R}^f_{sl}$.

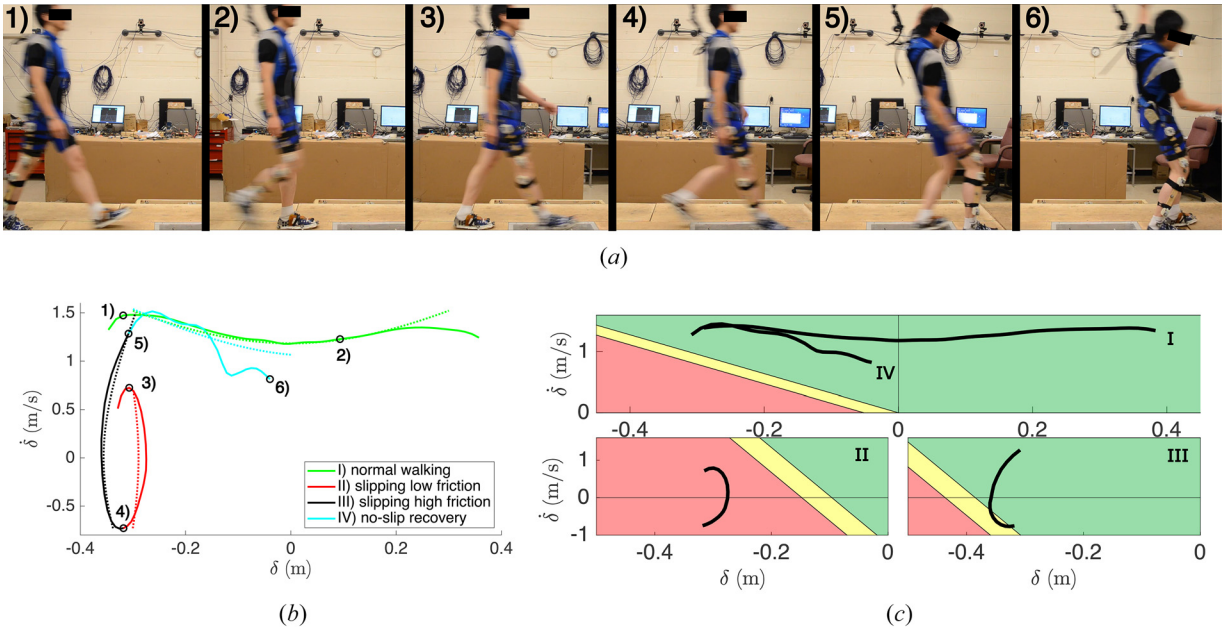

(*a*) (*b*) (*c*)

Fig. 11 (*a*) Human subject during successful slip recovery: 1) and 2) normal walking gait; 3) start of slip on the right foot; 4) slipping foot transitions from the low to the high-friction ground; 5) the right foot stops slipping on the ground; 6) positioning the left foot to bring the CoM velocity to zero. (*b*) Successful slip recovery due to change in friction conditions. Solid lines represent experimental data and dotted lines represent simulation results. Abrupt increase of μ between red and black curves changes the trajectory of the manifold. (*c*) Top: periodic phase I and nonslip recovery phase IV are part of safe region without foot slip. Bottom left: during slip with $\mu = 0.1$ the walker enters the fall-prone region. Bottom right: change in the friction coefficient to $\mu = 0.4$ moves the boundary $\mathcal{B}^{\text{rf}}$ bringing the walker into a safe region.

starting with normal walking, continuing with slip and ending with successful slip recovery. Figure 11(*b*) shows the gait progression in the δ-$\dot{\delta}$ plane. The subject was able to successfully avoid falling backward, continued forward progression, stopped his slipping foot and ultimately came to a resting position. This was possible due to the change in friction conditions. Slip was initiated as the subject stepped onto the lubricant covered polymer part of the walkway with a low friction coefficient ($\mu \approx 0.1$). The slipping step was initiated near the end of the slippery surface and slipping continued until the foot reached the high-friction walkway with a high friction coefficient ($\mu \approx 0.4$), $\dot{\delta}$ increased and the slipping foot stopped, bringing the subject back to normal walk. We add the simulation results using the two-mass LIP model in Fig. 11(*b*). By the proposed design, the control input $u = u^{\max}$ is taken when slip starts. For the nonslip recovery, $u = -u^{\max}$ is used to bring the gait to stop. The simulation and the experimental results are in good agreement.

Figure 11(*c*) shows the regions corresponding to each part of the slip-recovery sequences. The region boundaries change whenever the standing foot starts and stops moving on the ground, as well as with the change in the friction coefficient μ. An increase in the friction coefficient effectively translates the $\mathcal{B}^{\text{rf}}$ and $\mathcal{B}^{\text{sr}}$ boundaries toward further negative δ, moving the current state in $\mathcal{R}^f_{sl}$ to safe region $\mathcal{R}^s_{sl}$. A noticeable deviation exists between the model and experimental results in phase IV in Fig. 11(*c*). This is due to the subject's swing foot intermittently touching the ground and initializing double-stance phase thereby modifying the CoP location.

We next look into one trial where the subject was unable to recover under foot slip. Figure 12(*a*) shows a consecutive series of gait snapshots when a subject attempted but failed balance

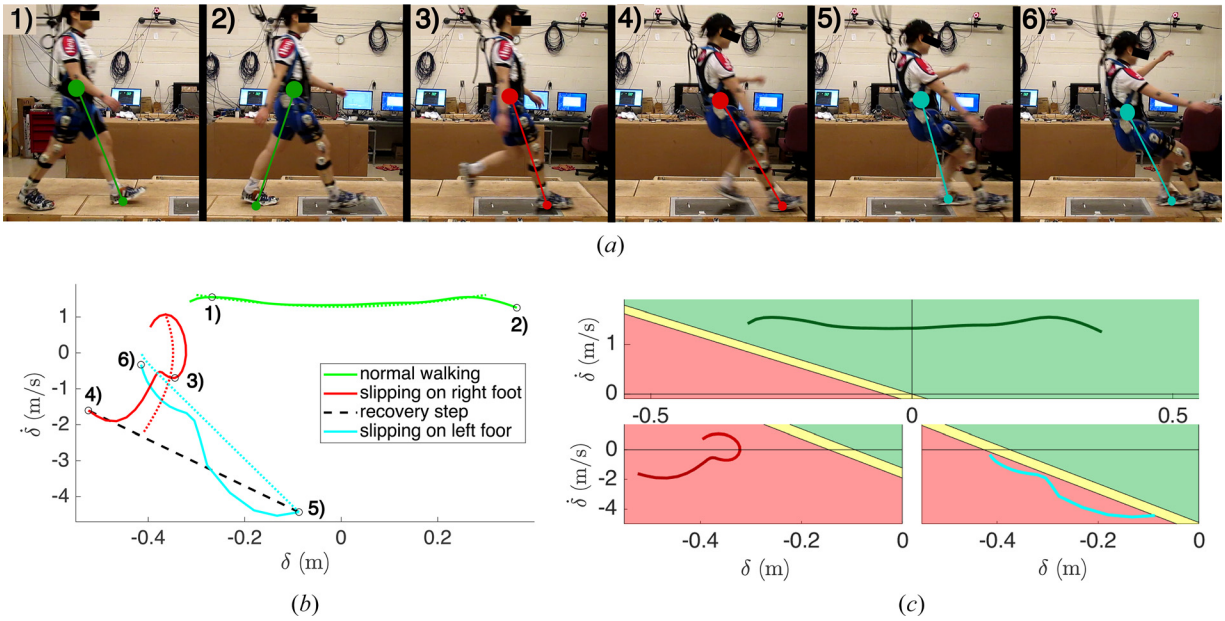

Fig. 12 (*a*) Human subject during unsuccessful slip recovery: 1) normal walking gait; 2) start of slip; 3) and 4) slipping on the right foot; 5) left leg touches the ground and becomes standing leg, continuing slip on the left leg; 6) falling gait. (*b*) Severe slip with unsuccessful recovery. Solid lines represent experimental data and dotted lines represent simulation results. Each of the marked points matches one of the snapshots in (*a*). (*c*) Unsuccessful recovery and the corresponding recoverability regions. Each curve matches one part of the gait in (*b*). Top: periodic walking gait without foot slip. Bottom left: slipping gait with $\mu = 0.1$. Bottom right: slipping gait with $\mu = 0.4$.

recovery. The subject walked with normal nonslip gait when they encountered a change of foot/ground friction condition, causing the right foot to start slipping; see snapshot 3) in the figure. The subject attempted to recover by taking an additional step with the left foot; see the two-mass LIP sketches in snapshots 4) and 5) in Fig. 12(*a*). At the moment of the heel strike, the left foot was already moving relative to the ground, and the subject continued to slip on the left foot. As the subject was unable to recover and the CoM moved vertically toward the ground, the safety harness system stopped the movement to avoid any injury; see snapshot 6) in Fig. 12(*a*) for subject's fallen state.

Figure 12(*b*) shows both the simulation and experimental results in the δ-$\dot{\delta}$ plane. Periodic walking and initial stages of slip are similar to the previous successful recovery case. In the later stages of slip, at the moment of snapshot 3), some perturbations happened probably due to motion near to the edge of the slippery platform or by subject's reaction to the unexpected slip. The subject continued the recovery sequence by taking a recovery step. A step is denoted as an instantaneous jump in the configuration of the model from snapshots 4) to 5) in Fig. 12(*b*). While the horizontal velocity of CoM was continuous and remained unchanged in the transition from snapshots 4) to 5), the left foot was moving faster than the right foot, thereby further decreasing $\dot{\delta}$. Figure 12(*c*) shows all three segments of gait progression phases with relation to the recoverability regions. It is expected that the periodic gait and slipping on the right foot are completely within regions $\mathcal{R}^{s}$ and $\mathcal{R}^{f}$, respectively. After the recovery step, the region boundaries changed as the left foot contacts nonslippery part of the walkway. While this transition shifted the region boundaries, the gait remained within $\mathcal{R}^{f}$ and the subject was still unable to recover.

6.2 Discussion. The multi-subject results in Fig. 10(*a*) show that normal walking gaits exhibit the expected shape of conjugate hyperbola while the slipping dynamics leads to backward fall as predicted theoretically in Fig. 2. Both normal walking and slipping gaits show notable variability between different subjects. Subject-specific parameters such as the mass ratio r_m or the CoM height z contribute insignificantly toward the variability. Instead, the differences between subjects can be explained by the variability in subjects' self-selected step length and walking speed.

Comparing the theoretical predictions to the experimental results, it is not surprising that the deviation is most notable at the boundaries of each trajectory portion, where the walker's gaits transit among different regions or exhibit double-stance phase. In particular, the double-stance phase of the gait introduces challenges when determining the CoP location and then δ. The CoP is confined to the support polygon which is significantly larger during the double-stance phase compared to the single-stance phase. The increased uncertainty in the CoP location and consequently δ leads to discrepancies between the simulation and experimental results during the double-stance phase of the gait. Fortunately, the double-stance phase is only a small fraction (e.g., 10–20%) of the entire walking gait cycle duration and therefore, the above-mentioned discrepancy is not significant. In order to completely achieve reliable modeling during the double-stance slipping experiments, the subjects might need to be outfitted with pressure sensitive insoles or a similar device that can be used to reliably estimate the overall CoP location.

The modeling and recovery strategy could serve as a high level control design specifying u and thus the location of CoP. For practical application, this high level controller needs to be combined with an assistive musculoskeletal stimulation or exoskeleton devices to help prevent people from falling due to slip. Integration and extension of the presented recovery control with the wearable knee exoskeleton developed in Ref. [27] for slip-and-fall prevention is one of the ongoing research directions.

There are still some limitations of the proposed work. The two-mass model stems from the assumptions such as the constant CoM height and all of the mass being concentrated in discrete points. The comparison of simulation and human experiments suggests that these assumptions and simplifications be reasonable both for nonslip and slip gait recovery control. Relaxing the constant CoM height assumption would offer additional insight into analyzing and predicting slip dynamics and is a direction for future research. Another limitation of the study is that the influence of the upper extremities on slip recovery strategies is not explicitly

considered. It is possible to consider and replace the mass m_1 in the current model with a flywheel to explicitly model angular momentum contribution of upper limbs. This is another future research direction to extend the current model and control design.

7 Conclusions

The two-mass LIP model enabled us to explicitly study slip dynamics and offered an analytical tool to understand gait stability in the absence and presence of foot slip. Analytical solutions helped translate the problem of dynamic stability into geometric analysis of the motion manifolds. The balance recoverability concept was introduced based on the developed motion manifolds. The closed-form analytical formulation and correspondingly low computational burden made the recoverability framework useful for both gait analysis and balance recovery control. A controller was formulated to optimize efficiency when fall was not immanent. The simulation results have demonstrated the recoverability analysis and performance of balance recovery control under foot slip. We also applied the analyses to human subject experiments. All subjects' data were shown to be in accordance with the predictions by the modeling and recoverability framework. We are currently working on extension and experimental implementation of the work on a bipedal robotic walker.

Acknowledgment

The authors thank Professor Ye Zhao of Georgia Institute of Technology and the members of the Robotics, Automation and Mechatronics (RAM) Lab at Rutgers for their help.

Funding Data

- U.S. National Science Foundation (NSF) (Award No. CMMI-1762556; Funder ID: 10.13039/100000001).

References

[1] Ambrose, A. F., Paul, G., and Hausdorff, J. M., 2013, "Risk Factors for Falls Among Older Adults: A Review of the Literature," Maturitas, **75**(1), pp. 51–61.

[2] Heinrich, S., Rapp, K., Rissmann, U., Becker, C., and König, H.-H., 2010, "Cost of Falls in Old Age: A Systematic Review," Osteoporosis Intl,., **21**(6), pp. 891–902.

[3] Wang, Y., Bhatt, T., Liu, X., Wang, S., Lee, A., Wang, E., and Pai, Y.-C., 2019, "Can Treadmill-Slip Perturbation Training Reduce Immediate Risk of Over-Ground-Slip Induced Fall Among Community-Dwelling Older Adults?," J. Biomech., **84**, pp. 58–66.

[4] Wang, Y., Wang, S., Lee, A., Pai, Y.-C., and Bhatt, T., 2019, "Treadmill-Gait Slip Training in Community-Dwelling Older Adults: Mechanisms of Immediate Adaptation for a Progressive Ascending-Mixed-Intensity Protocol," Exp. Brain Res., **237**(9), pp. 2305–2317.

[5] Chambers, A. J., and Cham, R., 2007, "Slip-Related Muscle Activation Patterns in the Stance Leg During Walking," Gait Posture, **25**(4), pp. 565–572.

[6] Trkov, M., Chen, K., Yi, J., and Liu, T., 2019, "Inertial Sensor-Based Slip Detection in Human Walking," IEEE Trans. Automat. Sci. Eng., **16**(3), pp. 1399–1411.

[7] Westervelt, E. R., Grizzle, J. W., Chevallereau, C., Choi, J. H., and Morris, B., 2007, *Feedback Control of Dynamic Bipedal Robot Locomotion*, CRC Press, Boca Raton, FL.

[8] Trkov, M., Chen, K., and Yi, J., 2019, "Bipedal Model and Hybrid Zero Dynamics of Human Walking With Foot Slip," ASME J. Comput. Nonlinear Dyn., **14**(10), p. 101002.

[9] Ma, W.-L., Or, Y., and Ames, A. D., 2019, "Dynamic Walking on Slippery Surfaces: Demonstrating Stable Bipedal Gaits With Planned Ground Slippage," Proceedings of IEEE International Conference on Robotics and Automation, Montreal, QC, Canada, May 20–24, pp. 3705–3711.

[10] Chen, T., and Goodwine, B., 2021, "Robust Gait Design for a Compass Gait Biped on Slippery Surfaces," Robot. Auton. Syst., **140**, p. 103762.

[11] Pratt, J., Carff, J., Drakunov, S., and Goswami, A., 2006, "Capture Point: A Step Toward Humanoid Push Recovery," Proceedings of IEEE International Conference on Humanoid Robots, Genova, Italy, Dec. 4–6, pp. 200–207.

[12] Vukobratović, M., and Borovac, B., 2004, "Zero-Moment Point–Thirty Five Years of Its Life," Intl. J. Humanoid Robot., **01**(01), pp. 157–173.

[13] Chen, K., Trkov, M., Chen, S., Yi, J., and Liu, T., 2016, "Balance Recovery Control of Human Walking With Foot Slip," Proceedings of the American Control Conference, Boston, MA, July 6–8, pp. 4385–4390.

[14] Koolen, T., de Boer, T., Rebula, J., Goswami, A., and Pratt, J., 2012, "Capturability-Based Analysis and Control of Legged Locomotion, Part 1: Theory and Application to Three Simple Gait Models," Int. J. Robot. Res., **31**(9), pp. 1094–1113.

[15] Mihalec, M., and Yi, J., 2018, "Capturability of Inverted Pendulum Gait Model Under Slip Conditions," ASME Paper No. DSCC2018-9203.

[16] Zaytsev, P., Wolfslag, W., and Ruina, A., 2018, "The Boundaries of Walking Stability: Viability and Controllability of Simple Models," IEEE Trans. Rob., **34**(2), pp. 336–352.

[17] Kuo, A. D., 2007, "The Six Determinants of Gait and the Inverted Pendulum Analogy: A Dynamic Walking Perspective," Human Move. Sci., **26**(4), pp. 617–656.

[18] Komura, T., Nagano, A., Leung, H., and Shinagawa, Y., 2005, "Simulating Pathological Gait Using the Enhanced Linear Inverted Pendulum Model," IEEE Trans. Biomed. Eng., **52**(9), pp. 1502–1513.

[19] Schwind, W. J., 1998, "Spring Loaded Inverted Pendulum Running: A Plant Model," Ph.D. thesis, Univ. of Michigan, Ann Arbor, MI.

[20] Kwon, T., and Hodgins, J. K., 2017, "Momentum-Mapped Inverted Pendulum Models for Controlling Dynamic Human Motions," ACM Trans. Graph., **36**(4), pp. 1–14.

[21] Kajita, S., Kanehiro, F., Kaneko, K., Yokoi, K., and Hirukawa, H., 2001, "The 3D Linear Inverted Pendulum Mode: A Simple Modeling for a Biped Walking Pattern Generation," Proceedings of IEEE/RSJ International Conference on Intelligent Robots and Systems, Maui, HI, Oct. 29–Nov. 3, pp. 239–246.

[22] Mihalec, M., Zhao, Y., and Yi, J., 2020, "Recoverability Estimation and Control for an Inverted Pendulum Walker Model Under Foot Slip," Proceedings of IEEE/ASME International Conference on Advanced Intelligent Mechatronics, Boston, MA, July 6–9, pp. 771–776.

[23] Mihalec, M., Trkov, M., and Yi, J., 2021, "Recoverability-Based Optimal Control for a Bipedal Walking Model With Foot Slip," Proceedings of the American Control Conference, New Orleans, LA, May 25–28, pp. 1766–1771.

[24] Zhao, Y., Fernandez, B. R., and Sentis, L., 2017, "Robust Optimal Planning and Control of Non-Periodic Bipedal Locomotion With a Centroidal Momentum Model," Int. J. Robot. Res., **36**(11), pp. 1211–1242.

[25] Winter, D. A., 2009, *Biomechanics and Motor Control of Human Movement*, 4th ed., Wiley, New York.

[26] Trkov, M., Yi, J., Liu, T., and Li, K., 2018, "Shoe-Floor Interactions Human Walking With Slips: Modeling and Experiments," ASME J. Biomech. Eng., **140**(3), p. 031005.

[27] Chen, S., Stevenson, D., Yu, S., Mioskowska, M., Yi, J., Su, H., and Trkov, M., 2021, "Wearable Knee Assistive Devices for Kneeling Tasks in Construction," IEEE/ASME Trans. Mechatronics, **26**(4), pp. 1989–1996.